Reconfigurable Low Phase Noise RF Carrier Generation up to W-Band in Silicon Photonics Technology

Antonio Malacarne ⬤, Alessandra Bigongiari ⬤, Antonio D'Errico ⬤, Antonella Bogoni, *Member, IEEE*, and Claudio Porzi ⬤

Abstract—Reconfigurable radiofrequency (RF) signal generation in the 30–300 GHz range is attractive for many applications. W-band (75–110 GHz) is currently targeted by both wireless and satellite communications and similar frequency ranges are employed for on-board automotive radar systems. Distribution of high-precision and high-frequency synchronization signals in modern centralized radio access networks might be addressed by radio-over-fiber solutions, but the stringent phase noise (PN) requirements in case of broadband signals with high subcarriers density are not easily attainable through conventional electric-domain solutions. This article reports on the performance of a monolithically integrated silicon photonics (SiP) circuit employed for RF carrier synthesis. Up to sixfold frequency multiplication of an 18.5 GHz reference clock is demonstrated with low additional phase noise. The circuit includes a high-speed electro-optic phase modulator employed for optical frequency comb (OFC) generation and a tunable distributed feedback resonator (DFBR) filter for selecting the desired OFC harmonic. The beating of the OFC tone with the input laser mode in an off-chip photodiode generates the target RF carrier wave. By tuning the reference clock and the DFBR filter, reconfigurable frequency generation up to W-band and beyond is achieved. PN and time jitter (TJ) of the generated RF carriers are experimentally measured, demonstrating a similar performance as of an ideal frequency multiplier. The effect of the noise of DC sources employed for filter tuning is assessed and a counteracting solution is implemented. TJ robustness versus laser drifting is analyzed and the potential for up to elevenfold frequency multiplication (203.5 GHz) is shown.

Index Terms—Microwave photonics, millimeter-wave generation, networks synchronization, silicon photonics, waveguide Bragg gratings.

I. INTRODUCTION

SEVERAL emerging broadband low-latency applications in wireless communication and sensor networks will operate in the high portion of the microwave band (e.g., above 20 GHz) and in the millimeter (mm) wave band (i.e., above 30 GHz), up to the sub-THz region (i.e., above 100 GHz) [1]. The considerably larger usable bandwidth at such frequencies, compared with the sub-6 GHz legacy spectrum, translates into a higher data rate for telecom systems and better resolution for sensing applications. Following this ever-increasing demand for larger bandwidth, Wi-Fi standard 802.11ad already operates in the 60 GHz regime, achieving data rates up to 7 Gb/s [2], and 5 G aims at providing data rates up to 10 Gb/s and above [3]. The 5 G New Radio (NR) standard has adopted in its Frequency Range two (FR2) the use of contiguous frequencies in the ranges of 24.25 - 29.50 GHz, 37-43.5 GHz, and 47.2–52.6 GHz [4]. The US Federal Communications Commission has allocated a portion of the V-band (40 - 75 GHz), formerly designed for mm-wave radar research, for high-capacity unlicensed wireless systems [5]. In addition, various sub-ranges of W-band (75 - 110 GHz) have been allocated as "lightly licensed" bands for multi-gigabit wireless communications and satellite communications, and the automotive market is investing substantial amounts of efforts for on-board radar sensors in the 77 - 81 GHz range [6].

The proliferation of services requiring high-speed connections in mobile wireless systems resulted in the definition of the centralized radio access network (C-RAN) architecture. In C-RANs, most of the baseband unit (BBU) processing functions of a traditional base station (BS) are moved away from the antenna cell site and shifted to a centralized location to maximize the bandwidth availability per single user and optimize the network's resources. This solution allows sharing the BBUs between multiple remote radio heads (RRHs), to which they are connected through a fiber-optic "fronthaul" network segment [7]. As the carrier frequency of the wireless system moves toward the mm-wave band, a densification of the cells is expected for facing the corresponding larger propagation loss [8], [9] and exploiting efficient frequency re-use [10]. For distributed sensors networks, radio over fiber (RoF) techniques can also be conveniently adopted [11].

One of the significant challenges in current 5 G C-RANs is related to the generation and distribution of high-precision

reference clock signals for network synchronization [12]. Multicarrier modulation techniques (such as orthogonal frequency division multiplexing, OFDM) employed in wireless mobile communications require a continuous-wave (CW) clock for multiplexing/demultiplexing the individual carriers with sufficient precision for not affecting the system performance [13]. The phase noise (PN) requirements in such operation become more and more stringent as the spacing between carriers is reduced, as for the high-bit-rate 5 G applications [14]. Additionally, coordination between the carrier frequency of multiple RRHs allows for effective deployment of multiple-input-multiple-output (MIMO) and carrier aggregation techniques, similarly supporting high data throughput in 5 G systems. In a currently deployed solution, the local oscillator (LO) generating the CW carrier frequency at the RRH is synthesized through phase-locked loops (PLLs) that synchronize to the baseband clock of received digitized samples of the RF signal. This approach suffers however from the time jitter introduced on the sampled data by the fronthaul link [15] as well as from the random PN generated by different PLLs at different RRHs, preventing accurate frequency coordination. An alternative solution would be distributing a single reference clock signal from the BBU to the RRHs by embedding a time transfer protocol functionality in the fronthaul [12]. High-resolution distributed sensor/radar networks share a similar need for a precise clock reference coordinating MIMO systems [16]. Electronic synthesizers for millimeter wave signals typically require multistage frequency multiplication and amplification chains as well as filtering and matching elements between the different stages [17], [18]. For instance, in [17] a ×9 frequency multiplier is used for generating a millimeter wave clock in the 92-96 GHz, although its excess PN prevents reaching the performance of an ideal frequency multiplier. In [18], where an eightfold multiplication is achieved reaching a 104 GHz-frequency, a careful noise analysis of each microwave device reveals how the main PN performance limitation comes from RF nonlinear frequency multipliers. A direct multiplication factor as high as 15 in an avalanche diode for generating signals in the W-band around 94 GHz and approaching the theoretical PN limit is reported in [19]. However, to support both the widely different input and output signal frequencies, the device operates as a resonant cavity which limits the tuning of the synthetized signal within about 2 GHz.

Microwave photonics approaches are based on heterodyne detection of two laser carriers at different wavelengths in a high-speed photodiode (PD) [19], [20], and are becoming increasingly appealing. Their main advantages include broad bandwidth and a high degree of reconfigurability. Furthermore, a simplified and economically sustainable distribution of a centralized clock source (e.g., located at the BBU in a C-RAN) to multiple RRHs can be efficiently supported over the fiber-optic network link. To minimize the complexity and power consumption of the RRH architecture, high-speed PDs operating at zero bias with bandwidth up to more than 100 GHz, as recently demonstrated [20], can be conveniently employed. However, solutions based on independent lasers sources (LSs) suffer from the relative phase and frequency fluctuations of the two optical carriers. According to 3GPP standard, the precision of the RF carrier frequency value

must be 50 - 100 parts per billion, which may be challenging to guarantee in case of different aging or temperature drift of the sources. For the sake of generating stable RF signals with low PN, the two optical tones at the PD input should exhibit a high degree of correlation, allowing for implementing noise cancellation schemes based on the coherence of the phase fluctuations [21]. This feature can be achieved by generating the beating tones through electro-optic modulators (EOMs) driven by a common reference clock signal. A proper configuration of the EOMs, optionally in conjunction with filtering elements, can be exploited to isolate two high-order modulating sidebands at its output, and realize frequency multiplication of the input reference signal after photodetection [22]–[24]. This approach suffers however from partial suppression of spurious modulator harmonics, which produce undesired components in the output RF spectrum. To improve the spectral purity of the frequency multiplied signal, highly selective filtering of the beating terms out of a coherent optical frequency comb (OFC) originating from a single LS through electro-optic modulators (EOMs) and driven by a high-purity reference RF clock at a lower frequency can be used [25]. An excellent phase noise characteristic up to the THz region has been demonstrated in this way by making use of commercial bulk-optics devices [25], [26]. By realizing such functionality within a photonic integrated circuit (PIC), the costs of the system could be drastically reduced, enabling its viable deployment in practical applications. This is for instance realized in [27] using a narrowband photonic-integrated filter that processes an off-chip OFC signal. In that case, the maximum output frequency is however limited by the periodic response of the filter, exhibiting a free spectral range (FSR) of 12.5 GHz.

Recently, we demonstrated the generation of mm-wave band RF carriers using a PIC realized in CMOS-compatible silicon-on-insulator (SOI) technology that allowed reconfigurable selection of the optical tones from an input OFC using a FSR-free filtering technique [28]. The results from a slightly modified architecture, in which the OFC source is additionally embedded within the same monolithic SOI PIC, have also been preliminarily presented in [29] and [30]. Although this latter scheme halved the maximum attainable spacing between selected pair of tones from the OFC compared to the architecture of [28], a frequency multiplication of an 18.5 GHz local oscillator (LO) up to 92.5 GHz was successfully demonstrated. Here, we provide further details on the circuit's operation with complete PN and time jitter analysis and discuss the possibility of further extending the photonic-integrated RF clock synthesizer range beyond the mm-wave band. A large degree of reconfigurability for the generated mm-wave band frequency is enabled trough a tuning combination of both the photonic integrated filter and of a low-frequency reference clock.

II. RF FREQUENCY MULTIPLICATION WITH SOI PIC

The schematic operation of the proposed PIC for frequency multiplication of a reference LO signal is reported in Fig. 1, and described in the following. The light from a LS entering the PIC is split into two paths through an optical splitter (OS). On one path, the light is delivered to a phase modulator (PM),
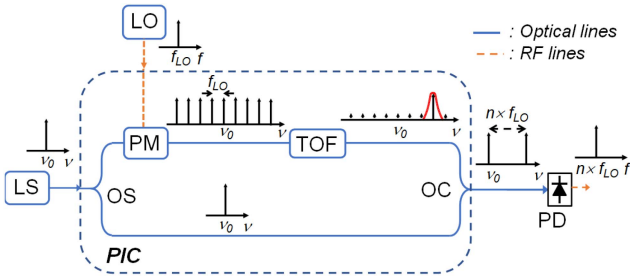
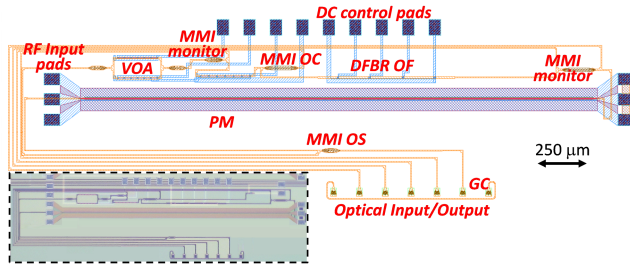Fig. 1. Schematic operation of the photonic-integrated RF clock source.

Fig. 2. Mask Layout and micrograph of the RF clock synthesizer PIC.

Fig. 3. Experimental setup for comprehensive phase noise characterization of the on-chip SOI RF synthesizes.

performed through on-chip grating couplers (GCs) for vertical alignment with a fiber array.

III. EXPERIMENTAL RESULTS

The experimental setup employed to test the PIC is reported in Fig. 3. The light from a distributed feedback (DFB) LS with an emission power of 14 dBm is injected into the PIC after a polarization controller (PC) for maximizing the GC coupling efficiency. An RF synthesizer (Synth) generates the continuous wave reference clock LO signal at 18.5 GHz. An RF amplifier boosts the PM driving signal power level at 27 dBm. The DC voltage for reverse biasing the SiP modulator pn-junction is provided by a source meter (SM) coupled to the LO clock through a bias-tee. The PIC temperature is kept constant during the measurements by a Peltier cell controlled by thermistor-based feedback.

A. SiP Phase-Modulator-Based OFC Characterization

The present section focuses on the stand-alone performance of clock frequency multiplication based on OFC generation through the SiP PM. The PM monitor output port from the PIC has been connected to a programmable wave-shaper (WS) filter based on LCoS technology, as illustrated in the setup of Fig. 3. The WS is configured to realize a dual passband transfer function, with frequency transmission peaks arbitrarily selecting tone pairs from the OFC. Subsequent heterodyne reception in a 100 GHz-bandwidth PD thus generates RF carriers centered at $N \times 18.5$ GHz, being N a positive integer determined by the order of the WS output tones. The PN power spectral density (PSD) of the generated RF carrier at the PD output is then measured with a signal source analyzer (SSA) using the setup illustrated in Fig. 3. A chain of two Erbium-doped fiber amplifiers (EDFAs) is employed between the comb monitor output and the PD. This allows for compensating both the PIC optical insertion loss and the large electrical losses of the harmonic mixers in the microwave downconverter, which amount to about 60 dB. The mixers are indeed required to overcome the 7 GHz bandwidth

driven by the LO clock with a suitably large voltage level for generating an OFC spanning several octaves at its output. A photonic integrated tunable optical filter (TOF) is then used to select a single tone out from the OFC and ensure strong suppression of all the remaining spectral components. An optical coupler (OC) then recombines the isolated comb tone with the optical carrier emerging from the second output of the input OS, and the composite signal is delivered to a high-speed PD at the circuit output. At the PD output, an RF carrier wave is generated at the beating frequency given by the detuning between the LS optical carrier and the selected OFC harmonic. Tuning the filter for selecting different comb tones allows synthesizing CW RF carriers at integer multiples of the original LO frequency.

The circuit has been realized in SOI technology through standard DUV lithography using a multi-project wafer service [31]. The corresponding mask layout and the fabricated PIC picture are reported in Fig. 2. The silicon photonics (SiP) PM employed for OFC generation has a 3 dB bandwidth of about 20 GHz when operating in carrier-depletion mode with a typical reverse bias voltage of about 3.5 V for maximized number of comb tones. The photonic-integrated TOF is implemented with a high-order distributed feedback resonator (DFBR) [32], realizing a coupled-cavity filter within a waveguide Bragg grating structure. Such compact wire-like geometry is particularly suitable for realizing narrow passband windows within relatively wide stop-band regions, as demanded by OFC demultiplexing [33]. The OC and OS elements are realized with multi-mode interference (MMI) devices. An additional MMI structure placed between the PM and the TOF is employed to monitor their output individually. Also, a variable optical attenuator (VOA) is inserted on the carrier path for controlling its amplitude and optimizing RF signal generation efficiency at the PD. Light coupling is
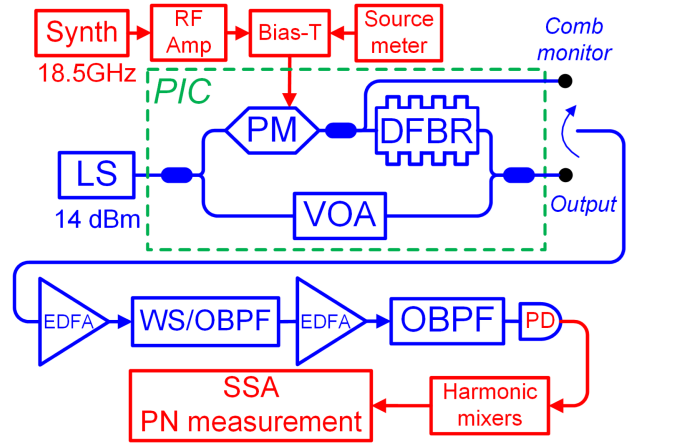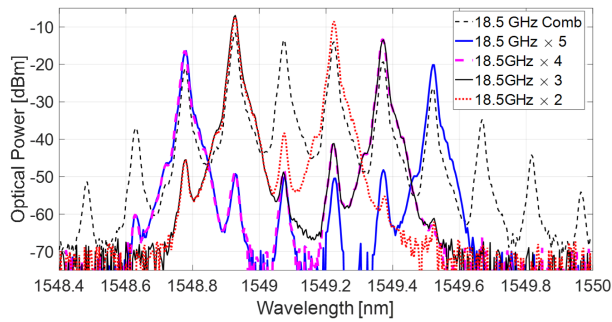
Fig. 4. WS input and output spectra. The input OFC (dashed black) is generated from the SiP PM. Different WS settings for comb tone selection corresponding to various multiplication factors of the baseline LO frequency of 18.5 GHz are shown.

of the SSA and extend the measurement range up to 110 GHz while guaranteeing the proper operative conditions in analyzing PN performance. However, for most practical applications such as millimeter-wave signal distribution in C-RANs, a single optical amplification stage is expected to be sufficient [34], [35], and hybrid on-chip integration of III-V semiconductor optical amplifiers (SOAs) [36] also represents an option for reducing the system costs and footprint. An optical bandpass filter (OBPF) is also used before the PD to band-limit the amplified spontaneous emission noise from the EDFAs chain. The PN has been measured in the range 1 kHz–40 MHz of frequency offset from the carrier under test. The upper limit has been chosen according to the requirements of modern wireless communication applications and considering the maximum detuning from the carrier of 40 MHz that is supported by the available SSA. On the other hand, PN contributions below 1 kHz, typically due to thermal and mechanical instabilities, can be compensated in practical applications by analog or digital carrier/phase recovery techniques.

The optical spectrum of the OFC generated by the SiP PM when driven with an RF power of 27 dBm (before the probe stage connecting the modulator electrodes) and reverse-biased at about 3.5 V is shown in Fig. 4. Different WS settings corresponding to the selection of tones pairs spaced by 37, 55.5, 74, and 92.5 GHz are also illustrated, corresponding to a frequency multiplication factor of 2, 3, 4, and 5, respectively, of the 18.5 GHz LO frequency. The original input laser wavelength is 1549.1 nm, corresponding to the central comb tone never selected by the WS. For benchmarking purposes, the PN performance of each generated RF carrier has been compared with the case in which the OFC source is replaced by a commercial Lithium Niobate (LiNbO$_3$) bulk PM. Although a fair comparison of the experimental results would require maintaining the same level of the relevant tones at PD input, a reasonable approximation is provided by keeping the same overall comb power as observed at the output port of the PIC PM monitor, i.e., −6 dBm, that is ensured through proper optical attenuation. This is justified by observing a similar spectral response for the integrated and external modulator that guarantees similar optical power for all the tones of interest as well as of the optical signal-to-noise ratio (OSNR) at the PD input for the two measurement cases.
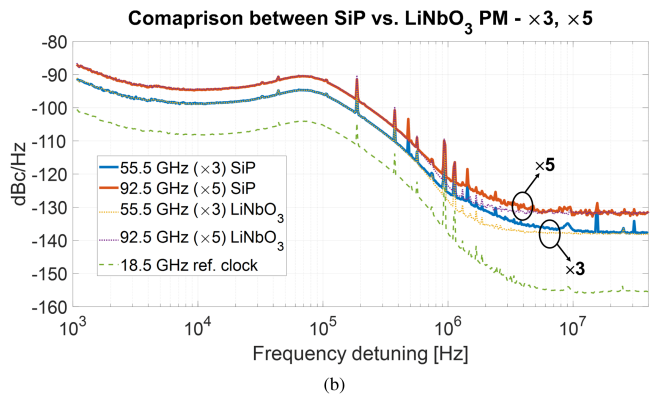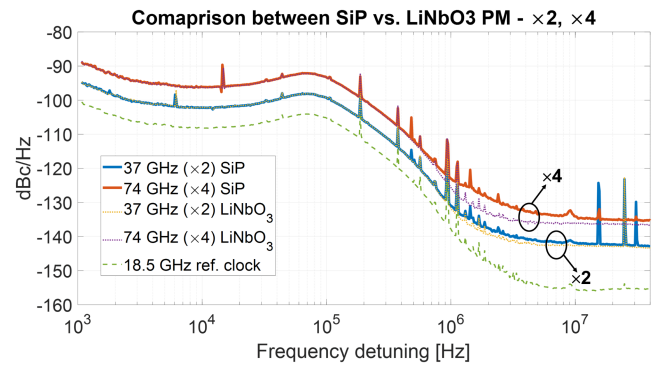

Fig. 5. Measured phase noise (PN) power spectral density (PSD) vs frequency detuning from the generated 37, 55.5, 74 and 92.5 GHz RF carriers through frequency multiplication of the 18.5 GHz reference local oscillator (LO) driving either a SiP or LiNbO$_3$ PM. (a) Frequency multiplication factors N=2 and N=4 are compared to the PN PSD of the baseline LO frequency. (b) Frequency multiplication factors N=3 and N=5 are compared to the PN PSD of the baseline LO frequency.

The comparison between the PN PSD curves measured for different frequency multiplication factors, N, for both SOI and LiNbO$_3$ PM cases is shown in Fig. 5(a) and (b), respectively. To facilitate plots interpretation, multiplication factors N = 2 and N = 4 are plotted separately from factors N = 3 and N = 5. As shown from the plots, for frequency offsets up to 1 MHz from the corresponding carrier frequency, SiP and LiNbO$_3$ PMs exhibit almost identical PN performance. The measured PN PSD in [dBc/Hz] increases with the multiplication factor N as 20log10 (N), in accordance to theory. For instance, the PN PSD at 18.5 GHz and 92.5 GHz (i.e., N = 5) shows a 14 dB difference. The PN PSD floors for higher frequency offsets (i.e., > 10 MHz) are given by the different sensitivity limits performed by the instrument at the available signal power and OSNR.

A second standard relevant metric for evaluating the quality of an RF clock signal is the root-mean-square (RMS) time jitter (TJ), which has been measured for each generated RF tone in the range between 1 kHz and 40 MHz. The corresponding results are illustrated in Fig. 6, indicating an RMS TJ almost constant at any level of N. In this case, the measurements confirm that both the SiP and LiNbO$_3$ PM schemes essentially act as an ideal frequency multiplier adding negligible noise to the reference oscillator frequency (N=1). Apart from the measurement uncertainty, the slightly decreasing trend of the measured TJ
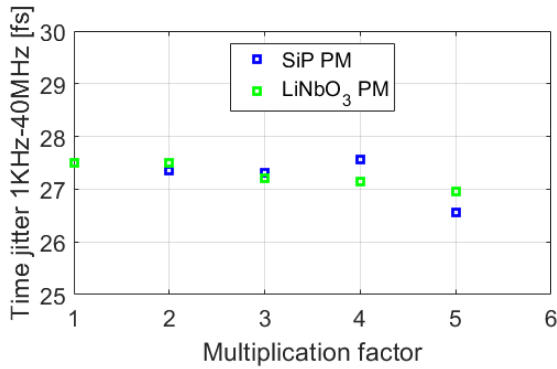
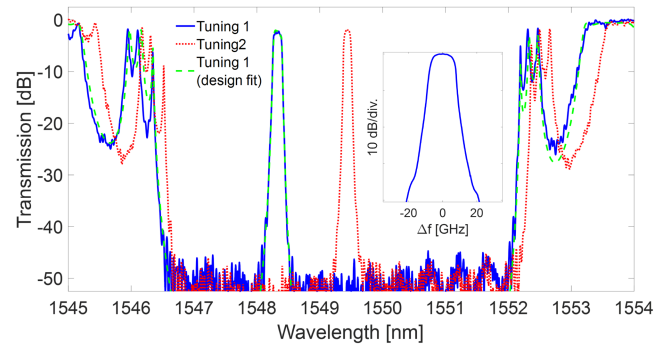Fig. 6. Root-mean-square time jitter calculated from traces of Fig. 5.

Fig. 7. Distributed feedback resonator (DFBR) filter spectral transmission. Inset: details of passband window.
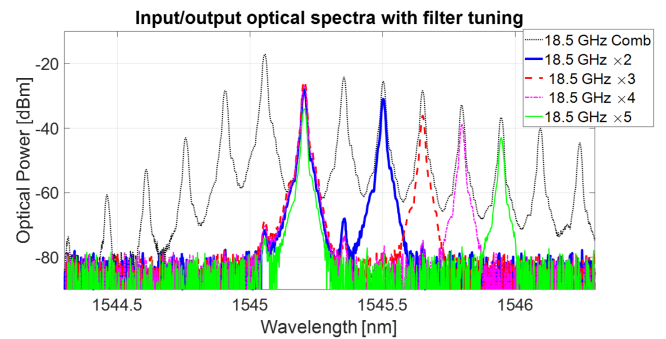

Fig. 8. OFC spectrum from SiP PM and PIC output spectra corresponding to different frequency multiplication factors after carrier-selected tone beating in the PD.

value as the multiplicative factor N increases is ascribed to constant disturbances, whose weight decreases by scaling up the analyzed frequency. It is worth noting that, in Fig. 5, for a given multiplication factor, the PN PSD for both SiP and LiNbO$_3$ PM cases tend to the same floor level, even though the roll-off is slightly slower for the signal emerging from the SOI PIC as the frequency offset increases. This issue is ascribed to the different electro-optic effects exploited in the SOI and LiNbO$_3$ PM, i.e., carrier depletion in a pn junction and Pockels effect, respectively. Nevertheless, the reported PN PSD floors lower than −130 dBc/Hz represents a significant improvement when compared with state-of-the-art electronics-based frequency synthesizers [37]–[39]. However, the described approach based on bulky and expensive LCoS technology for OFC tones filtering is unsuitable for cost-effective photonics-based RF clock source deployment in emerging C-RANs and distributed sensor networks. The following section addresses the effects of including OFC generation and filtering within a monolithic SOI PIC on generated RF carrier performance.

B. Full On-Chip Reconfigurable RF Carrier Generation up to the W-Band

Monolithic on-chip reconfigurable RF carrier generation is then implemented following the scheme of Fig. 3. A tunable LS with emission power of 14 dBm is employed in this case. Either a positive or negative harmonic tone from the SiP PM-based OFC generator can be now selected from a tunable 4th-order DFBR filter, which is then recoupled with the original carrier, as described above. The scheme can be straightforwardly updated for selecting comb tones located at opposite detuning from the LS carrier by generating the OFC before splitting the signal into two different branches, each comprising a TOF [28]. Alternatively, a DFBR with dual-wavelength passband transmission characteristic can be designed [40], at the expense of the reconfigurability of the RF synthesizer. The tuning of the DFBR multi-cavity filter is realized by controlling through local micro-heaters (MHs) the optical path of the cavities created by inserting four phase shift sections between five waveguide Bragg Grating mirrors (BGMs), as detailed in [32], [41]. The spectral transmission of the device is shown in Fig. 7, illustrating a sharp passband window with an out-of-band rejection of nearly 50 dB

within a 6.5 nm-wide stopband region defined by the BGMs bandwidth. The passband details reveal a −1 dB BW of about 11 GHz, an insertion loss of about 2.5 dB, and an attenuation of about 40 dB at a detuning of 20 GHz from the center frequency (roll-off: 2.5 dB/GHz). Two different tuning settings of the filter are shown in the figure, along with the numerical fit for the case named "Tuning 1".

Fig. 8 shows the optical spectrum of the generated OFC (dotted thin black line) and that of the signal at the PIC output for different cases of selected comb tones by the DFBR filter. The VOA on the lower arm of the PIC is set to maximize the AC power at the PD output [42], which improves the sensitivity of the PN measurement. An optical bandpass filter (OBPF) is placed after the first EDFA at the PIC output to limit amplified spontaneous emission noise. The traces at the PIC output correspond to a frequency multiplication factor of the LO frequency ranging from 2 to 5 for a synthesized RF clock up to 92.5 GHz. The associated thermally tuned DFBR filter spectral responses are shown in Fig. 9, where the power dissipated from the four MHs, P_{MHs}, for each tuning setting is also reported. The corresponding PN PSD for each generated carrier frequency has then been measured and compared with the PN of the LO synthesizer at the baseline 18.5 GHz frequency, see Fig. 10. The curves show that the observed excess noise at different offset values from the carrier for each generated carrier is only partially due to the frequency multiplication mechanism. The PN traces of the high-frequency signals show indeed a
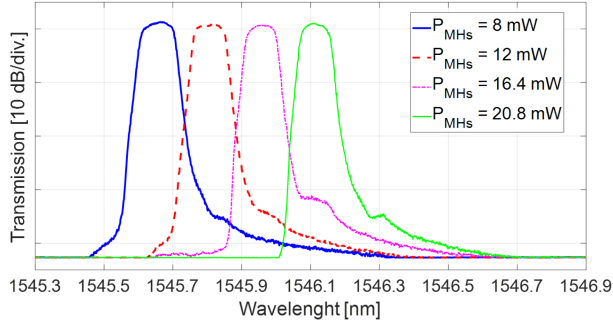
Fig. 9. DFBR filter responses corresponding to frequency multiplication factors of the 18.5 GHz clock frequency from ×2 up to ×5.

Fig. 11. PN PSD of the generated RF carrier at a frequency of 37, 55.5, 74 and 92.5 GHz, and the LO clock signal at 18.5 GHz, in the case of entire on-chip operation and low-pass filter (LPF), applied to the MHs driving signals.
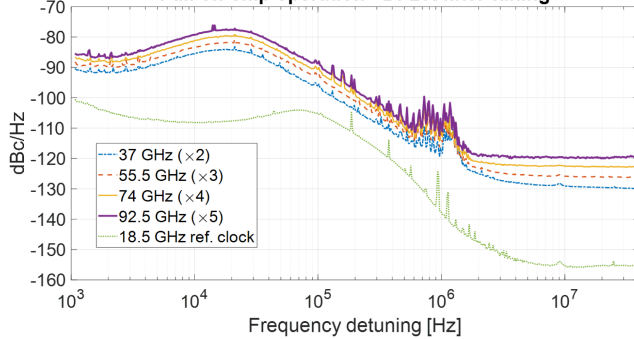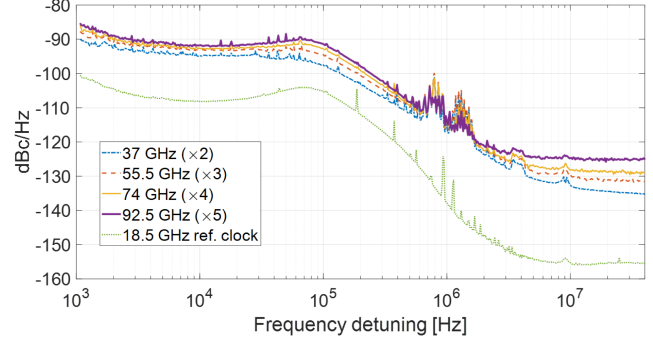

Fig. 10. PN PSD of the generated RF carrier waves at 37, 55.5, 74 and 92.5 GHz, and of the LO signal at 18.5 GHz, for the case of entirely on-chip operation.
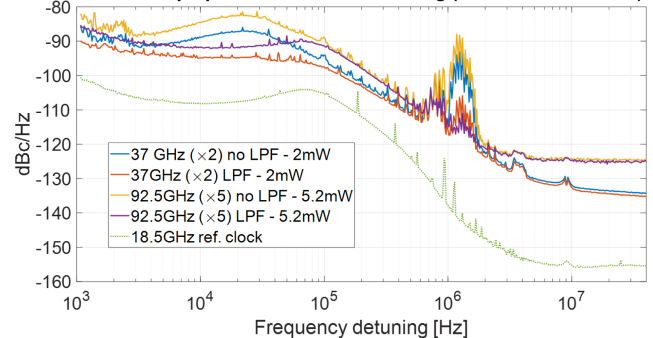

Fig. 12. Comparison of PN PSD of the generated RF carrier at 37 and 92.5 GHz, with and without LPF applied to the SMs.

different shape when compared to that of the reference baseline clock. For all the plots, a noise spike with slow roll-off appears at about 20 kHz, along with a noise term with relatively large PSD around 1 MHz, both ascribed to additional PN contribution related to harmonic selection through the DFBR filter that was not present in the WS case. A more careful inspection of the setup revealed that the SMs providing the control voltage to the MHs for DFBR filter tuning exhibited pronounced noise terms over the same frequency range of the observed spikes in the PN PSDs of Fig. 10. For the noise term at around 20 kHz, a root mean square voltage of 30 mVpp was measured through a real-time oscilloscope. Such random temperature fluctuations at the heaters translate into the instability of the DFBR filter central frequency, which in turns produces slight oscillations in the phase of the selected optical tone due to the non-flat phase response of physical filters. The terms at around 1 MHz are well above the cut-off frequency of the thermo-optic effect employed for filter tuning and, as such, are strongly attenuated in respect to the 20 kHz term, although its magnitude at the SM output is higher than the one at 20 KHz. Nevertheless, they are still clearly visible in the PN PSD of the output signal and its contribution to the calculated TJ is not negligible, as discussed ahead. This is also in accordance with the observed increase of the noisy spectral components around 20 kHz and 1 MHz as the filter is tuned to select higher-order OFC harmonics. Indeed, as the

power dissipated on the MHs increases to attain more extensive tuning ranges, the SM noise contribution increases following the quadratic power-voltage relation.

A second set of PN measurements has then been performed to verify further the frequency-selective excess PN contribution arising from the SMs driving the DFBR filter. A low-pass filter (LPF) with a cut-off frequency of about 7 Hz has now been inserted between the SMs output signals and the DC probes contacting the MHs electrodes. The results, reported in Fig. 11, show a clear improvement compared to the case of Fig. 10 without LPF. For better comparison, the PN PSD for two-fold and five-fold frequency multiplication for either the issues with or without LPF applied to the SM output signals are reported in the plots in Fig. 12.

The calculated RMS TJ for each generated RF carrier from the various PN PSD measurements is summarized in Fig. 13. The full on-chip operation with DFBR filter tuning with and without LPF applied to the SMs (dashed pink square and dashed blue squares, respectively) is compared with that obtained when an external WS is used to select the two beating tones from the SiP PM (solid red square). The measured TJ of the employed 18.5 GHz reference clock is also shown.

As expected, full on-chip operation with DFBR tuning without low-pass filtering of the control signals corresponds to the highest values for the measured TJ, above those of an ideal
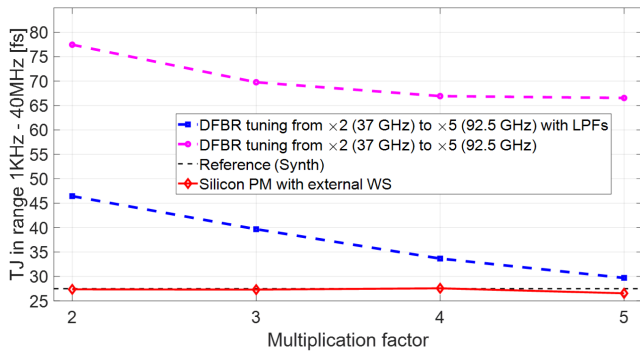
Fig. 13. Summary of RMS TJ for the different considered operating conditions of the RF synthesizer.
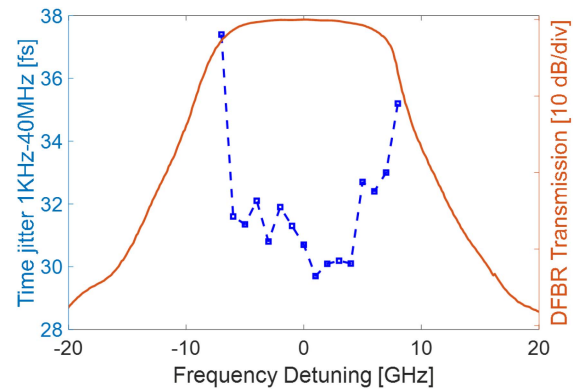

Fig. 14. TJ versus detuning between laser carrier and DFBR filter central frequency, in case of 92.5 GHz generation and overall dissipated power from MHs of 8 mW. DFBR spectral transmission is also shown.
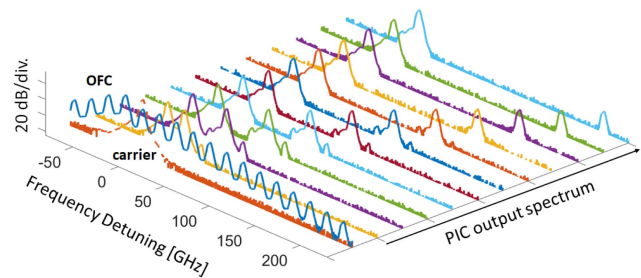

Fig. 15. Spectra of the input laser carrier, SiP PM OFC, and PIC output spectra for a selected sideband carrier detuning up to 203.5 GHz with 18.5 GHz steps.
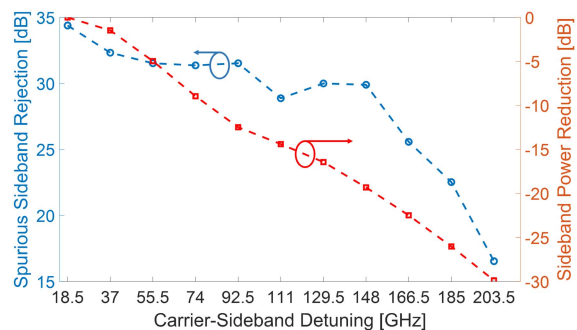

Fig. 16. Summary of the spurious sideband rejection/OSNR and relative power drop in the selected sideband for the traces of Fig. 15.

frequency multiplier. This is the trade-off for avoiding expensive and bulky off-chip WS equipment in liquid crystal on silicon (LCoS) technology, which would lead to the lowest TJ values. Nevertheless, proper cleaning of the control signal effectively allows to approach the ideal case. The residual difference with respect to the reference clock, together with its decreasing trend for higher multiplication factors, suggests the presence of some residual disturbance which is constant for each measurement (whose weight is more prominent for lower frequency multiplication factors). For the generation of 92.5 GHz, a TJ of 29.7 fs is measured using DFBR tuning and LPFs, compared to 27.5 fs in the case of the reference clock and 26.5 fs in the case of external optical filtering through a WS. The excess phase noise due to non-ideal MHs control signal can also be significantly reduced by tuning the LS for selecting different OFC harmonics while keeping the filter fixed at the lowest power tuning condition, as shown in [30]. This approach would also be advantageous for the particular case in which a relatively fast reconfiguration of the RF synthesizer is required, as the LPFs affect the DFBR tuning speed, which was demonstrated to be as fast as about 200 μs (limited by the cooling process) [43]. Also in this case, the solution represents a trade-off between system features and costs for the requirement of fast tunable LS.

As a final performance evaluation, the TJ of generated RF carrier wave has been monitored as a function of the detuning between the optical carrier and DFBR filter central frequency, to attest the system robustness to drifts of the laser frequency. The result is reported in Fig. 14, where the DFBR filter spectral response is also shown. Within a 10 GHz-wide detuning, approximately matching the −1 dB bandwidth of the filter, the deterioration of the TJ is below 10%. At a 15 GHz detuning, the value increases to 30% due to the steeper phase response of the filter at the passband edges. The measurement has been carried out at the lowest tuning power of the DFBR filter and setting the LS wavelength for generating an RF carrier at 92.5 GHz. An identical minimum TJ value of 29.7 fs, as in the last point of Fig. 13 in the presence of the LPF was obtained, confirming the effective removal of SM noise with this approach.

C. Extending RF Synthesizer Operation

From the spectral characterization of Fig. 7, it can be seen that the broad stop-band region of the DFBR filter can support

operation with OFCs extending over several hundreds of GHz. An example of isolated tone selection up to about 200 GHz is reported in Fig. 15. The input carrier, the 18.5 GHz-spaced OFC from the SiP PM and the PIC output spectra for up to elevenfold multiplication of the LO frequency are reported. For simplicity, the spectra have been taken by keeping fixed the filter frequency and tuning the laser carrier. The traces are plotted relative to the absolute carrier-to-sideband detuning value. Fig. 16 reports the summary of the performance for the various measurements in terms of spurious sideband rejection (or equivalently, the OSNR for the cases in which no spurious sideband is detectable at the PIC output), and of the roll-off of the selected harmonic power with respect to the first-order filtered harmonic case. Although a
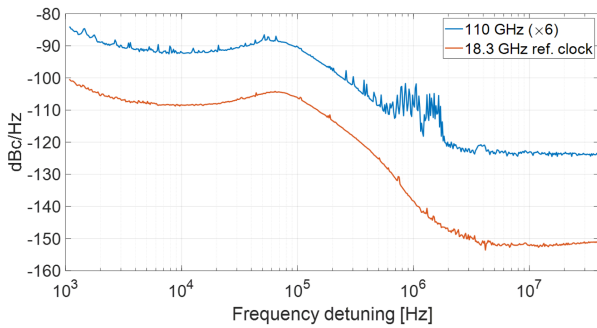
Fig. 17. PN PSD of generated RF carrier at frequency 109.8 GHz and of the 18.3 GHz reference clock.

sideband OSNR of 30 dB is still preserved at 148 GHz detuning, the main limitation for this simple single-PM-based OFC source is the drop of power associated with increasing the order of selected comb harmonics. It can be expected that operation in the sub-THz region (i.e. between 0.1 and 0.3 THz) or above would be supported with the proposed photonic-integrated architecture by using slightly more advanced OFC architectures like a dual-PM cascade [26], in combination with simultaneous filtering of both positive and negative harmonics from the OFC [28].

Since the maximum frequency for the signals accepted at the SSA input is 110 GHz, the final characterization of the sixfold multiplied LO reference clock has been performed by lowering its baseline rate to 18.3 GHz. The PN PSD of the resulting 109.8 GHz carrier frequency and the reference clock trace are depicted in Fig. 17. The deviation in dBc/Hz from the ideal offset between the two curves, i.e. 15.6 dB, is lower than 1.5 dB for frequency detuning lower than 600 kHz, confirming the potential of the proposed approach. The measurement floor for higher detuning values represents again the measurement's sensitivity due to the limited signal OSNR at such high order of selected harmonic. The corresponding TJ is 29.5 fs, slightly above the reference value of 25.4 fs for the baseline clock frequency. Through numerical processing and interpolation (not detailed here) of the blue curve in Fig. 17, it is calculated that, net of the residual additional PN term around 1 MHz, the resulting TJ at 109.8 GHz would be 25.9 fs. Therefore, with a most effective LPF at the SMs output, TJ performance can in principle reach the one of the reference clock. Finally, Fig. 18 shows the RF spectra plotted by the SSA in a 15 MHz span, verifying a good spectral purity of the generated 109.8 GHz carrier compared to the reference 18.3 GHz one. The reported power of -52.3 dBm represents the RF carrier power at the harmonic mixer output.

In the next Section the possible alternatives for on-chip integration of the laser source, optical amplification stages and broadband photodiodes are discussed, together with associated benefits and realization challenges.

IV. DISCUSSION

The coupling loss and compactness of the circuit could be reduced by on-chip integration of the laser source. Hybrid integration of III-V laser source on SOI PICs has been thoroughly investigated in the last recent years, and can be achieved using
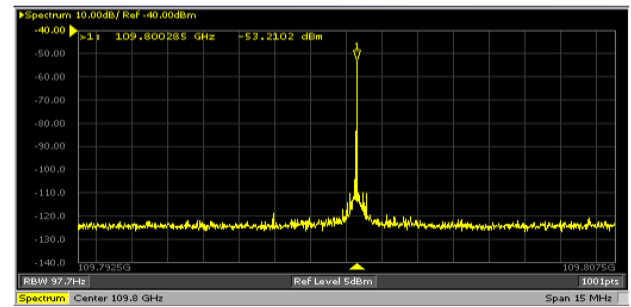
(a)
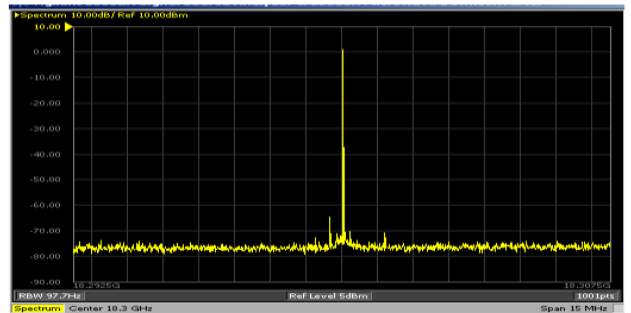
(b)

Fig. 18. Signal spectrum analyzer (SSA) traces for (a) the generated RF carrier at 09.8 GHz and (b) the 18.3 GHz reference clock.

bonding, ethero-epitaxy, or transfer printing techniques. Bonding of III-V semiconductor gain regions can provide high-power low threshold laser sources [44], which would be advantageous in the proposed photonic-integrated RF synthesizer for decreasing RF input-output conversion loss, attaining large OSNR at PD input and consequently low PN floor. However, the requirement of handling the gain sections complicates the fabrication process [45]. Epitaxial growth of III-V material on a silicon substrate is on the other hand a cost-effective approach, and improvements in the laser linewidth in the O-band have been achieved by making use of quantum dots for the gain medium and lattice matching buffer layers [46]. Transfer printing methods offer on the other hand the possibility of a larger parallel integration with respect to bonding techniques, with a higher process maturity than direct III-V on SOI epitaxy [47].

For applications not requiring fiber transport of the millimeter wave carrier, on-chip SiP PDs could be employed to provide an RF output port of the PIC [28]. State-of-the-art Ge PDs can reach bandwidth values up to about 70 GHz [48] and [49], while larger values can be attained in graphene-based devices [50]. To rise the optical power at the PD to sufficiently large levels, on-chip amplification using hybrid integration of semiconductor optical amplifiers in the SiP circuit could be employed [36].

V. CONCLUSION

Up to sixfold photonics-based frequency multiplication of an $\sim$ 18.5 GHz reference clock is achieved within a monolithic silicon photonics circuit. In the scheme, a thermally tunable distributed feedback resonator (DFBR) bandpass filter is responsible for selecting an isolated harmonic out from an on-chip

generated optical frequency comb driven by the reference clock. The generated RF carrier at the output of an external photodiode (PD) exhibited limited additional phase noise (PN) for clock frequency multiplication factors from two to six, with respect to ideal frequency multiplication. The residual excess noise is mainly ascribed to fluctuations of DC signals employed for tuning the DFBR filter. By low-pass filtering the outputs of the DC sources, the performance of the integrated RF clock synthesizer is further improved, achieving a time jitter (TJ) of 29.5 fs for the maximum generated frequency of 109.8 GHz against a TJ of 25.4 fs for the clock reference at 18.3 GHz. An analysis of TJ robustness with respect to laser wavelength variations reveals that the TJ increment stays within 10% for a ±5 GHz carrier drift. Finally, the possibility of generating an RF carrier up to 203.5 GHz (elevenfold reference frequency multiplication) is detailed in terms of spurious sideband rejection and power of the harmonics in the generated optical spectrum. These results illustrate the potentials of the proposed technique for improved operation by using advanced architectures for both a more efficient OFC generation and a filtering strategy maximizing the achievable spacing between the selected optical harmonics. Concerning RF clock frequency multiplication up to W-band, the proposed solution exhibits PN performance similar to full RF solutions and a comparable required input RF power [19]. However, due to the high conversion loss from input to output RF power, requiring additional optical/electrical amplification, the overall power consumption is expected to exceed that of full RF solutions. Nevertheless, the proposed technique offers a unique mix of features, such as wide reconfigurability for the output frequency and the possibility for effectively delivering high-speed and high-accuracy millimeter-band synchronization signals to multiple remote peripherals located up to a few tens of kilometers from a common base station, through low-loss optical fiber links. Additionally, a high performance comparable with that attained using bulk optic components is demonstrated within an ultra-compact photonic integrated circuit having a footprint of less than 2 mm^2 and realized with CMOS-compatible silicon on insulator technology.

REFERENCES

[1] S. Tripathi, N. V. Sabu, A. K. Gupta, and H. S. Dhillon, "Millimeter-wave and terahertz spectrum for 6G wireless," in *6G Mobile Wireless Networks*. Berlin, Germany: Springer, 2021, pp. 83–121.

[2] T. Nitsche et al., "IEEE 802.11ad: Directional 60 GHz communication for multi-gigabit-per-second Wi-Fi," *IEEE Commun. Mag.*, vol. 52, no. 12, pp. 132–141, Dec. 2014.

[3] J. G. Andrews et al., "What will 5G be?," *IEEE J. Sel. Areas Commun.*, vol. 32, no. 6, pp. 1065–1082, Jun. 2014.

[4] Accessed: Apr. 2022. [Online]. Available: https://www.3gpp.org/Dyna Report/38-series.htm

[5] Accessed: Apr. 2022. [Online]. Available: https://www.govinfo.gov/content/pkg/CFR-2002-title47-vol1/pdf/CFR-2002-title47-vol1-sec15-255.pdf

[6] Accessed: Feb. 2022. [Online]. Available: https://www.etsi.org/deliver/etsi_en/302200_302299/302264/02.01.01_30/en_302264v020101v.pdf

[7] A. Pizzinat, P. Chanclou, F. Saliou, and T. Diallo, "Things you should know about fronthaul," *J. Lightw. Technol.*, vol. 33, no. 5, pp. 1077–1083, 2015.

[8] Y. Xing and T. S. Rappaport, "Propagation measurements and path loss models for sub-THz in urban microcells," in *Proc. IEEE Int. Conf. Commun.*, 2021, pp. 1–6.

[9] A. Al-Saman et al., "Survey of millimeter-wave propagation measurements and models in indoor environments," *Electronics*, vol. 10, no. 14, 2021, Art. no. 1653.

[10] N. Al-Falahy and O. Y. K. Alani, "Network capacity optimisation in millimetre wave band using fractional frequency reuse," *IEEE Access*, vol. 6, pp. 10924–10932, 2018.

[11] A. Malacarne, S. Maresca, F. Scotti, P. Ghelfi, G. Serafino, and A. Bogoni, "Coherent dual-band radar-over-fiber network with VCSEL-based signal distribution," *J. Lightw. Technol.*, vol. 38, no. 22, pp. 6257–6264, Nov. 2020.

[12] D. P. Venmani, Y. Lagadec, O. Lemoult, and F. Deletre, "Phase and time synchronization for 5G C-RAN: Requirements, design challenges and recent advances in standardization," *EAI Endorsed Trans. Ind. Netw. Intell. Syst.*, vol. 5, no. 15, Aug. 2018, Art. no. e3.

[13] A. G. Armada, "Understanding the effects of phase noise in orthogonal frequency division multiplexing (OFDM)," *IEEE Trans. Broadcast.*, vol. 47, no. 2, pp. 153–159, Jun. 2001.

[14] C. Browning et al., "Gain-switched optical frequency combs for future mobile radio-over-fiber millimeter-wave systems," *J. Lightw. Technol.*, vol. 36, no. 19, pp. 4602–4610, Oct. 2018.

[15] T. A. Diallo et al., "Jitter impact on mobile fronthaul links," in *Proc. Opt. Fiber Commun. Conf.*, 2014, pp. 1–3.

[16] A. M. Haimovich, R. S. Blum, and L. J. Cimini, "MIMO radar with widely separated antennas," *IEEE Signal Process. Mag.*, vol. 25, no. 1, pp. 116–129, Dec. 2007.

[17] A. Hati, C. Nelson, and D. Howe, "PM noise measurement at W-band," *IEEE Trans. Ultrason. Ferroelect. Freq. Control.*, vol. 61, no. 12, pp. 1961–1966, Dec. 2014.

[18] R. Bara-Maillet et al., "Microwave-to-millimeter-wave synthesis chain phase noise performance," *IEEE Trans. Ultrason. Ferroelect. Freq. Control.*, vol. 62, no. 10, pp. 1895–1900, Oct. 2015.

[19] L. Song and M. Zhao, "The research of W-band high order frequency multiplier based on avalanche diode," *Prog. Electromagn. Res. Lett.*, vol. 72, no. 10, pp. 45–53, 2018.

[20] T. Umezawa et al., "Bias-free operational UTC-PD above 110 GHz and its application to high baud rate fixed-fiber communication and W-band photonic wireless communication," *J. Lightw. Technol.*, vol. 34, no. 13, pp. 3138–3147, 2016.

[21] G. Qi et al., "Phase-noise analysis of optically generated millimeter-wave signals with external optical modulation techniques," *J. Lightw. Technol.*, vol. 24, no. 12, pp. 4861–4875, Dec. 2006.

[22] P.-T. Shih et al., "Optical millimeter-wave signal generation via frequency 12-tupling," *J. Lightw. Technol.*, vol. 28, no. 1, pp. 71–78, Jan. 2010.

[23] M. Hasan and T. Hall, "Rebuttal to "photonic microwave generation with frequency octupling based on a DP-QPSK modulator"," *IEEE Photon. Technol. Lett.*, vol. 28, no. 16, pp. 1794–1794, Aug. 2016.

[24] H. Zhang, Z. Dong, X. Wu, and K. Zhang, "Generation of frequency-eightfold millimeter-wave with optical carrier suppression by using one single-drive modulator," in *Proc. Int. Symp. Intell. Signal Process. Commun. Syst.*, 2017, pp. 353–356.

[25] A. R. Criado et al., "Continuous-wave sub-THz photonic generation with ultra-narrow linewidth, ultra-high resolution, full frequency range coverage and high long-term frequency stability," *IEEE Trans. Terahertz Sci. Technol.*, vol. 3, no. 4, pp. 461–471, Jul. 2013.

[26] S. Jia et al., "THz wireless transmission systems based on photonic generation of highly pure beat-notes," *IEEE Photon. J.*, vol. 8, no. 5. Oct. 2016, Art. no. 7905808.

[27] Z. Geng et al., "Photonic integrated circuit implementation of a sub-GHz-selectivity frequency comb filter for optical clock multiplication," *Opt. Exp.*, vol. 25, no. 22, pp. 27635–27645, 2017.

[28] C. Porzi, F. Falconi, M. Sorel, P. Ghelfi, and A. Bogoni, "Flexible millimeter-wave carrier generation up to the sub-THz with silicon photonics filters," *J. Lightw. Technol.*, vol. 39, no. 24, pp. 7689–7697, Dec. 2021.

[29] A. Malacarne et al., "Reconfigurable low-phase noise frequency generation up to 92.5 GHz in a monolithically integrated silicon photonics circuit," in *Proc. 47th Eur. Conf. Opt. Commun.*, 2021, doi: 10.1109/ECOC52684.2021.9605957.

[30] A. Malacarne, F. Falconi, A. Bigongiari, A. D'Errico, A. Bogoni, and C. Porzi, "Silicon photonics circuit for tunable low-phase noise RF generation up to W-band," in *Proc. Int. Topics Meet. Microw. Photon.*, 2021, pp. 1–4.

[31] Accessed: Jul. 2022. [Online]. Available: https://europractice-ic.com/technologies/photonics/imec/

[32] C. Porzi, G. J. Sharp, M. Sorel, and A. Bogoni, "Silicon photonics high-order distributed feedback resonators filters," *IEEE J. Quantum Electron.*, vol. 56, no. 1, Feb. 2020, Art. no. 6500109.

[33] C. Porzi et al., "Integrated silicon-on-insulator optical comb demultiplexer for elastic optical networks," *IEEE Photon. Technol. Lett.*, vol. 32, no. 14, pp. 867–870, Jul. 2020.

[34] B. Zhu et al., "Large-area low-loss fibers and advanced amplifiers for high-capacity long-haul optical networks," *J. Opt. Commun. Netw.*, vol. 8, no. 7, pp. A55–A63, 2016.

[35] B. Wang, L. Peng, and P.-H. Ho, "Energy-efficient radio-over-fiber system for next-generation cloud radio access networks," *EURASIP J. Wireless Commun. Netw.*, vol. 2019, no. 1, pp. 1–8, 2019.

[36] K. Van Gasse, R. Wang, and G. Roelkens, "27\,db gain III-V-on-silicon semiconductor optical amplifier with >17 dBm output power," *Opt. Exp.*, vol. 27, no. 1, pp. 293–302, 2019.

[37] G. Liu, A. Trasser, and H. Schumacher, "A 64-84-GHz PLL with low phase noise in an 80-GHz SiGe HBT technology," *IEEE Trans. Microw. Theory Techn.*, vol. 60, no. 12, pp. 3739–3748, Dec. 2012.

[38] G. Hasenaecker et al., "A SiGe fractional-N frequency synthesizer for mm-Wave wideband FMCw radar transceivers," *IEEE Trans. Microw. Theory Techn.*, vol. 64, no. 3, pp. 847–858, Mar. 2016.

[39] A. I. Hussein, S. Vasadi, and J. Paramesh, "A 50–66-GHz phase-domain digital frequency synthesizer with low phase noise and low fractional spurs," *IEEE J. Solid-State Circuits*, vol. 52, no. 12, pp. 3329–3347, Dec. 2017.

[40] D. Novak, Z. Ahmed, R. B. Waterhouse, and R. S. Tucker, "Signal generation using pulsed semiconductor lasers for application in millimeter-wave wireless links," *IEEE Trans. Microw. Theory Techn.*, vol. 43, no. 9, pp. 2257–2262, Sep. 1995.

[41] C. Porzi, G. J. Sharp, M. Sorel, and A. Bogoni, "High-contrast, flat-top, silicon-photonics passband optical filters with high-order phase-shifted Bragg gratings," in *Proc. 44th Eur. Conf. Opt. Commun.*, 2018, doi: 10.1109/ECOC.2018.8535293.

[42] B. Hraimel et al., "Optical single-sideband modulation with tunable optical carrier to sideband ratio in radio over fiber systems," *J. Lightw. Technol.*, vol. 29, no. 5, pp. 775–781, Mar. 2011.

[43] F. Falconi, C. Porzi, A. Malacarne, F. Scotti, P. Ghelfi, and A. Bogoni, "UWB fastly-tunable 0.5–50 GHz RF transmitter based on integrated photonics," *J. Lightw. Technol.*, vol. 40, no. 6, pp. 1726–1734, 2022.

[44] A. Fang et al., "Electrically pumped hybrid AlGaInAs-silicon evanescent laser," *Opt. Exp.*, vol. 14, no. 20, pp. 9203–9210, 2006.

[45] R. Helkey, A. Saleh, J. Buckwalter, and J. Bowers, "High-performance photonic integrated circuits on silicon," *IEEE J. Sel. Topics Quantum Electron.*, vol. 25, no. 5, pp. 8300215, Sep./Oct. 2019.

[46] Y. Wan et al., "1.3 μm quantum dot-distributed feedback lasers directly grown on (001) Si," *Laser Photon. Rev.*, vol. 14, no. 7, 2020, Art. no. 2000037.

[47] J. Zhang et al., "Transfer-printing-based integration of a III-V-on-silicon distributed feedback laser," *Opt. Exp.*, vol. 26, no. 7, pp. 8821–8830, 2018.

[48] S. Lischke et al., "High bandwidth, high responsivity waveguide-coupled germanium p-i-n photodiode," *Opt. Exp.*, vol. 23, no. 21, pp. 27213–27220, 2015.

[49] H. Chen et al., "−1 v bias 67 GHz bandwidth Si-contacted germanium waveguide pin photodetector for optical links at 56 Gbps and beyond," *Opt. Exp.*, vol. 24, no. 5, pp. 4622–4631, 2016.

[50] D. Schall et al., "Record high bandwidth integrated graphene photodetectors for communication beyond 180 Gb/s," in *Proc. Opt. Fiber Commun. Conf.*, 2018, pp. M2I–4.